JACS
JOURNAL OF THE AMERICAN CHEMICAL SOCIETY

ARTICLE

pubs.acs.org/JACS

High-Quality Manganese-Doped Zinc Sulfide Quantum Rods with Tunable Dual-Color and Multiphoton Emissions

Zhengtao Deng,[†,‡] Ling Tong,[§] Marco Flores,[‡] Su Lin,[†,‡] Ji-Xin Cheng,[§,#] Hao Yan,[†,‡] and Yan Liu*[,†,‡]

[†]The Biodesign Institute and [‡]Department of Chemistry and Biochemistry, Arizona State University, Tempe, Arizona 85287, United States

[§]Department of Chemistry and [#]Weldon School of Biomedical Engineering, Purdue University, West Lafayette, Indiana 47907, United States

S *Supporting Information*

ABSTRACT: We report a simple, fast and green phosphine-free colloidal chemistry to synthesize high-quality wurtzite-type Mn-doped ZnS quantum rods (QRs) with tunable diameters (1.6−5.6 nm), high aspect ratios (up to 50), variable Mn doping levels (0.18−1.60%), and high quantum yields (up to 45%). The electron paramagnetic resonance spectra with modeling reveal the successful doping of paramagnetic Mn^{2+} ions in the host ZnS QRs. The Mn-doped ZnS QRs demonstrate tunable dual-color (orange and blue) emissions by tuning the doping levels and UV excitation wavelengths. The orange emission with long decay lifetime (3.3 ms) originates from the doped Mn^{2+} states, while the blue emission with fast decay lifetime (0.31 ns) is attributed to the QR surface states. The bright two- and three-photon excitation upconversion luminescence from the Mn-doped ZnS QRs have been observed using tunable near-infrared femtosecond laser. Our strategy provides a versatile route to programmably control the optical properties of anisotropic semiconductor nanomaterials, which may create new opportunities for photonic devices and bioimaging applications.

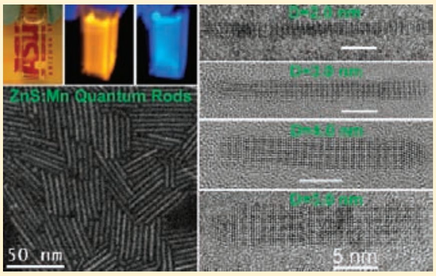

INTRODUCTION

Quantum rods (QRs) are one-dimensional quantum-size semiconductor crystallites with diameters comparable to the Bohr exciton radius (e.g., 2.5 nm for ZnS) and lengths ranging from 5 to 100 nm.[1−5] QRs share some important properties with spherical quantum dots (QDs), such as broad excitation spectra, size-dependent narrow emission bands, and resistance to photobleaching. Moreover, QRs might offer some advantages over QDs, such as larger absorption cross sections, faster radiative decay rates, more substantial Stokes shifts, linearly polarized emissions, and capablity of functionalization at distinct sites with multiple binding moieties.[4−7] These distinct features make QRs highly desirable materials for a wide range of applications ranging from bioimaging and biosensors to nanodevices.[8−10]

Paramagnetic-ion-doped semiconductors or diluted magnetic semiconductors have attracted significant attention in the past few years.[11−16] Doping enhances the properties of semiconductors by providing a powerful method to control their significant optical, electronic, transport, and spintronic properties.[13,16] Mn-doped zinc chalcogenide QDs have been explored as alternatives to CdSe QDs, with the advantages of lower toxicity, larger Stokes shifts, and enhanced thermal and environmental stability.[17−25] The synthesis of Mn-doped ZnS nanorods (diameter ≥ 5 nm) by solvothermal method[26,27] and Mn-doped ZnSe nanowires by single-source precursor method[28] have also been reported. However, the synthesis of high-quality Mn-doped ZnS QRs, characterized by sharp exciton absorption peaks, finely tunable and uniform diameters, tunable doping levels, and high quantum yields, is still a great challenge.

Herein, we demonstrate a simple, fast, and "green" phosphine-free colloidal chemistry for synthesis of high-quality wurtzite-type Mn-doped ZnS QRs with uniform diameters that are finely tunable from 1.6 to 5.6 nm, and variable Mn doping levels ranging from 0.18% to 1.6%. To our knowledge, this is the first example of colloidal synthesis of high-quality Mn-doped ZnS QRs with sharp exciton absorption peaks, finely tunable and uniform diameters, and high quantum yields up to 45%. In addition, our Mn-doped ZnS QRs demonstrate tunable dual-color (orange and blue) emissions and bright multiphoton (two- and three-photon) excitation luminescence, which may create new opportunities for photonic device and bioimaging applications.

RESULTS AND DISCUSSION

Our synthesis of high-quality Mn-doped ZnS QRs is shown in Scheme 1. Air-stable and simple metal nitrate salts, $Zn(NO_3)_2$ and $Mn(NO_3)_2$, are employed as the metallic precursors, sulfur powder as the sulfur precursor, oleylamine as the solvent, 1-dodecanethiol as the capping ligand, and relatively short reaction times of 5−20 min. A series of QR samples, referred as QR1−QR8, were generated by varying the reaction time and the molar ratio of Mn/Zn precursors (see Table 1).

Received: December 7, 2010
Published: March 15, 2011

Table 1. Summary of Morphology Measurements from TEM, Mn-Doping Level Measurements from ICP-MS, and Optical Characterization of the Mn-Doped ZnS QR Samples; Initial Molar Ratio of Mn/Zn Precursors and Reaction Time Are Also Listed

QR sample No.	Reaction time (minutes)	Sample size (nm)	Initial Mn^{2+} concentrations (mol %)	Doped Mn^{2+} concentration (mol %)	First exciton absorption band (nm)
QR1	5	1.6 × 80	5	0.18	286
QR2	5	2.0 × 45	20	0.25	292
QR3	10	2.3 × 38	5	0.32	294
QR4	10	3.0 × 32	20	0.36	296
QR5	15	3.3 × 30	5	0.37	298
QR6	15	4.0 × 25	20	0.51	299
QR7	20	5.0 × 22	5	0.81	300
QR8	20	5.6 × 20	20	1.60	300

Scheme 1. Schematic Illustration Our Simple, Fast, and "Green" Phosphine-Free Colloidal Chemistry for Synthesis of high-quality Mn-Doped ZnS QRs

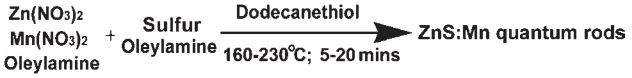

The morphology of the samples was revealed by transmission electron microscopy (TEM) and high-angle annular dark field scanning transmission electron microscopy (HAADF-STEM), which show the formation of high-quality QRs. Selected samples with diameters of 2.0, 3.0, 4.0, and 5.0 nm are depicted in Figure 1; enlarged and additional images for all the samples (QR1−QR8) are shown in the Supporting Information (Figures S1−S12). Each sample shows uniform diameters and lengths (histograms were shown in Figures S1, S2, S4−S7, S10, and S11). In some cases, these QRs prefer to self-assemble into close-packed three-dimensional (3D) superlattices with their long axes parallel to each other (Figure S12).

High-resolution TEM (HRTEM) study demonstrated well-resolved two-dimensional crystal lattices (Figure 2), indicating that the individual QRs are highly crystalline. The lattice spacings of 0.309 nm in the length direction and 0.327 nm in the width direction correspond to the (002) and the (100) planes, respectively, which are consistent with the wurtzite phase of ZnS (JCPDS Card No. 80-0007) and powder X-ray diffraction (XRD) measurement (Figure S13). The wurtzite phase is dominant in the QR samples, as illustrated by the structural models (Figure 2), while a small amount (<2%) of cubic zinc blende phase could also be observed. ZnS with hexagonal wurtzite and cubic zinc blende phases have several overlapping diffraction peaks, especially the (002), (110), and (112) peaks of wurtzite are close to the (111), (220), and (311) peaks of zinc blende. We speculate that the unique geometry of the QRs and the presence of Mn dopants, which can alter the crystal phase of the ZnS nanocrystals,[26] contributes to the hexagonal wurtzite phase of ZnS QRs. This also agrees with the previous report on the ultrathin Mn doped ZnSe quantum wires, which also shows a hexagonal wurtzite phase.[28]

The growth of anisotropic Mn-doped ZnS QRs, instead of spherical QDs, could be understood by a ligand controlled kinetic mechanism, which is similar to the growth of wurtzite-type CdSe QRs by manipulation of the growth kinetics.[1−3] Wurtzite-type ZnS is a member of the hexagonal crystal system and consists of tetrahedrally coordinated zinc and sulfur atoms that are stacked in an ABABAB pattern. Their anisotropic unit cells have large *c*-axis of 6.188 Å, and small identical *a*- and *b*-axis of 3.777 Å (JCPDS Card No. 80-0007). Nearly spherical faceted QDs that minimizes the total surface area is favored if the overall growth rate is slow. However, when the growth rate is fast using high monomer concentrations and optimal reaction temperatures, anisotropic QRs will grow with *c*-axis as their growth directions. The time-dependent morphology evolution of the Mn-doped ZnS QRs indicates that there exists an initial nucleation and fast longitudinal growth process; then followed by an aging process in which the long and thin QRs gradually grow shorter and wider (see Table 1). In addition, we obtained wider QRs (see Table 1) by increasing Mn^{2+} precursor concentration and keeping other reaction parameters the same, which indicates that the presence of Mn^{2+} dopants could also alter the growth kinetic of the QRs.

We used inductively coupled plasma mass spectrometry (ICP-MS) to determine the concentration of Mn^{2+} doped in the ZnS QR samples, i.e., the Mn^{2+} doping levels, that were between 0.18% and 1.60% for samples QR1−QR8 (Table 1). TEM-based energy-dispersive X-ray analysis (TEM-EDS) studies were also used to investigate the Mn^{2+} doping levels but with less accuracy (Figure S14). It is known that Mn^{2+} is a harder Lewis acid compared to Zn^{2+}.[17] Therefore, Mn^{2+} would be less reactive than Zn^{2+} if they were present at the same reaction environments. The Mn^{2+} doping levels showed a nonlinear correlation with the reaction time and QR diameters (Figure S15), which is due to the kinetic, not the thermodynamic, controlled QR growth process. The relative low doping levels (0.18−1.60%) of the Mn-doped ZnS QRs is attributed to their small diameters (1.6−5.6 nm), in contrast to the higher doping level (20%) for Mn-doped ZnS nanorods with a much larger diameter (~100 nm).[26]

To reveal the local environment of Mn^{2+} ions doped in the QRs, we performed the X-band electron paramagnetic resonance (EPR) spectroscopy study. As depicted in Figure 3, the EPR spectra corresponding to samples QR1, QR3, QR5, and QR7 exhibit well-resolved hyperfine splitting lines, which indicates the presence of the paramagnetic Mn^{2+} ions in the samples. We extracted a hyperfine coupling interaction of 192 MHz for the Mn^{2+} doped QRs samples and 267 MHz for free Mn^{2+} ions in aqueous solution (see Table S1), indicating that the hyperfine splitting of Mn^{2+} is strongly dependent on their local environments. This unambiguously confirmed the successful doping of paramagnetic Mn^{2+} ions in the ZnS crystal lattice.[12,25,29,30] Furthermore, we performed the simulations for the EPR spectra with a spin Hamiltonian containing a zero field splitting interaction, an electron Zeeman interaction with the applied magnetic field, and a hyperfine coupling interaction (see more details in

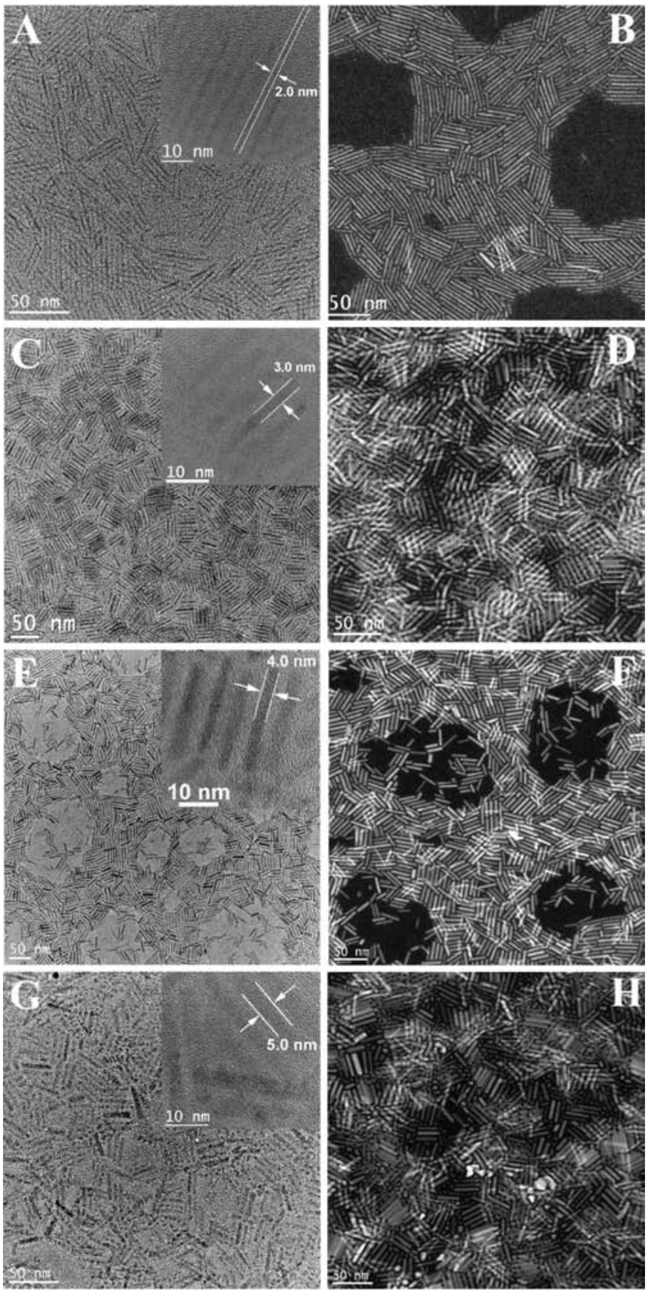

Figure 1. Transmission electron microscopy (TEM) and scanning transmission electron microscopy (STEM) images of QRs with diameters of ~2.0 (A,B), ~3.0 (C,D), ~4.0 (E,F), and ~5.0 nm (G,H), respectively. Insets (A, C, E, and G) are selected zoom-in TEM images of the several QRs.

Table S1 and Figures S16 and S17).[29] From the simulation, we identified four different scenarios that describe the different local environments of the doped Mn^{2+} in the ZnS QRs with various diameters and doping levels, labeled as M1, M2, M3, and M4 in the schematic diagram (Figure 3).

The EPR spectrum of the QR1 sample with the smallest diameter (1.6 nm), longest length (~ 80 nm), and the lowest doping level (0.18%) could be simulated very well using a single Mn^{2+} scenario of M1, which is isolated Mn^{2+} doped in the interior of the ultrathin ZnS QRs. This kind of Mn^{2+} is fully coordinated to the sulfur ions with a tetrahedral symmetry. Using the size and the doping level of QR1 depicted in Table 1 and assuming the Mn^{2+} ions distributed evenly along the longitudinal direction, the calculated Mn^{2+} ions per QR is ~7, and the calculated average distance between Mn^{2+} ions is ~10 nm. Thus, no interactions between the Mn^{2+} ions are expected. It is surprising that no surface Mn^{2+} (i.e., M2) but only symmetrically coordinated internal Mn^{2+} (i.e., M1) was observed for QR1 with an ultrathin diameter (1.6 nm), since a large fraction of the whole atoms of the QRs (>40%) is expected to be present on the surface. According to the "self-purification" effect[15,16] observed in ultra-small QDs, the Mn impurities tend to be repelled. This is because that the spherical QDs have very small interior volume, thus inner impurities can easily migrate to the surface and be excluded. In the case of anisotropic doped QRs, similar to the spherical QDs, the Mn^{2+} on the surface is unstable and would be repelled from the host QRs, as lowering the surface energy of the QRs is preferred rather than hosting another atom on the surface.[11,12] However, due to the large sizes (~80 nm) in the longitudinal direction, the host QRs may have enough interior volume to host the Mn^{2+} impurities with symmetric coordination. Therefore, only the internal symmetrically coordinated Mn^{2+} was found in the 1.6 nm QR1. These results indicated that we are capable of doping Mn^{2+} inside the ultrathin QRs with a magic-size (size <2 nm) diameter by a simple phosphine-free chemistry, which was not achieved before by other synthesis methods.

Sample QR3 has a larger diameter 2.3 nm and a higher doping level 0.32% as compared to QR1. The EPR study indicated that there exist both the surface Mn^{2+} (M2) with broken tetrahedral symmetry and the interior Mn^{2+} (M1) with tetrahedral symmetry. Further increasing QR diameters and Mn-doping levels, the Mn^{2+} ions doped in each QR will become closer (e.g., there are ~25 Mn^{2+} per QR with an average distance ~2 nm in QR5, and there are ~100 Mn^{2+} per QR with an average distance ~1.6 nm in QR7). As a result, weak dipole−dipole interactions (e.g., M3 in QR5) and strong exchange coupling interactions (e.g., M4 in QR7) between the doped Mn^{2+} ions show up, in addition to the M1 and M2 states (Figure 3; see SI section 5 for details of the EPR simulation). Our EPR study demonstrated not only the strong evidence of the existence of the paramagnetic Mn^{2+} ions doped in the ZnS QRs, but also the underlying information about the locations and interactions of these doped Mn^{2+} ions.

The as-prepared QRs samples dispersed in hexane are colorless and transparent under room light (see Figure S19). However, they show very high extinction in the UV region (see Figures S19 and S22). The UV−visible absorption spectra of the as-prepared samples with 500 times dilution are depicted in Figure 4. The Mn-doped ZnS QRs (QR1−QR7) exhibit sharp, first exciton absorption bands, reflecting their uniform size (diameter and length). This was achieved by terminating the QR growth in the "focusing of size distribution" regime.[31] The quality of the spectra is comparable to the best optical spectra of CdSe QRs or the Mn-doped ZnS QD counterparts in the literature.[1,3,12−14] The peak of the exciton absorption band gradually shifts from 286 to 300 nm (4.34−4.14 eV) as the QR diameter increases from 1.6 to 5.6 nm. The shifts of the first absorption exciton peaks from the bulk wurtzite ZnS are plotted against the diameter of the Mn-doped ZnS QRs, revealing a nearly quadratic dependence (See Figure S18). The blue shift of the band gap with narrowing the QRs could be explained by diameter-dependent 2D quantum confinement effect in QRs.[1]

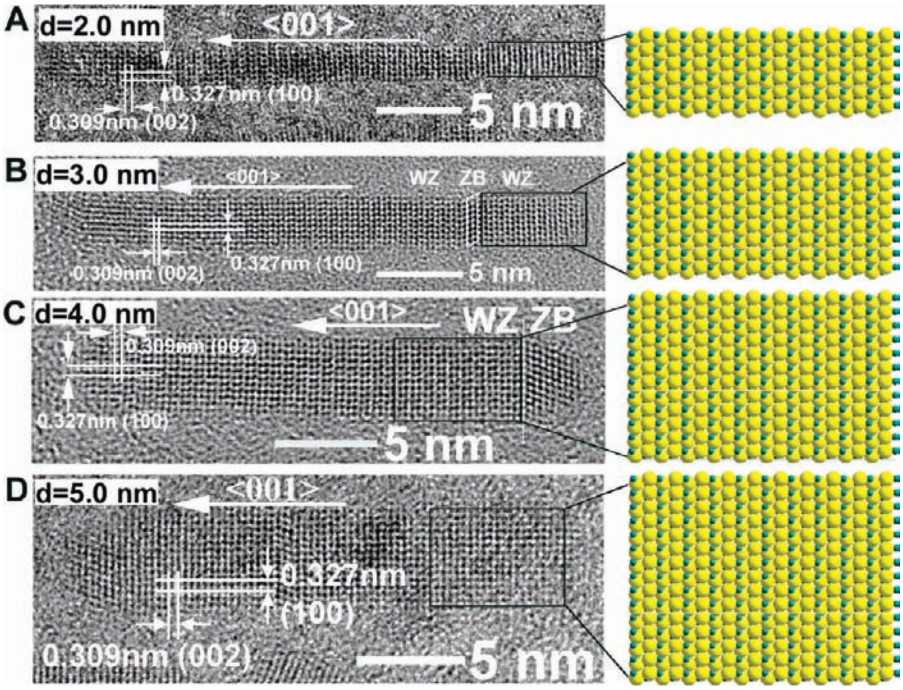

Figure 2. High resolution transmission electron microscopy (HR-TEM) images of Mn-doped ZnS QRs with diameters of ~2.0 (A), ~3.0 (B), ~4.0 (C), and ~5.0 nm (D) and their corresponding structural models of the indicated areas. For all the structural models, the projection is ⟨010⟩, the small cyan ball represents Zn or Mn atom and the large yellow ball represents S atom.

The photoluminescent (PL) emission spectra from the samples (QR1−QR7) all contain distinct orange bands centered at 585 nm (see Figure 4). These emission bands originate from the Mn^{2+} doping states,[25] indicating the successful doping of Mn^{2+} in the crystal lattice of the host ZnS QRs. In addition, the QR samples show the blue emission bands centered at 400 nm, which are attributed to the QR surface states.[32] As shown in Figure 4, with increasing Mn^{2+} doping levels and QR diameters from QR1 to QR7, the relative intensity of the blue bands to orange bands decreases, which is mainly due to the increasing intensity from the orange emission, while only small intensity changes (PL quantum yield ~3−8%) were observed from the blue emission. The above results suggest that the ratio of the dual-color emissions (orange and blue) of the Mn-doped ZnS QRs could be controlled by tuning the Mn doping levels of the QRs. It is worth to note that our previous work on undoped ZnS QRs and quantum wires only show blue emission band from the surface states, and no orange emission band from the Mn^{2+} impurity.[32] The lack of the orange emission band in the PL spectrum of the undoped ZnS QRs further supports the claim that the orange emission is derived from the Mn^{2+} impurity.

The tunable dual-color emissions of the Mn-doped ZnS QRs are further investigated by tuning the excitation wavelength (Figure 5, Figures S19−S22, and Movie S1). As an example, we excited QR4 with 300 nm UV, an intense orange emission band centered at 585 nm (with PL quantum yield of 45%, see Figure S23) and a weaker blue emission band centered at 400 nm (with PL quantum yield 3.4%, see Figure S23) were observed (the optical image shown in Figure 5A inset). The photoluminescent excitation (PLE) spectrum (black trace in Figure 5A) of the orange emission resembles its absorption spectrum (see Figure 4), indicating there exist an energy transfer from the host ZnS conduction band to the doped Mn^{2+} $^4T_1$ state. The decay lifetime of the orange emission is ~3.3 ms (Figure 5C) by measuring the phosphorescence decay using a microsecond flash lamp. The decay of the orange emission was also monitored on the 100 μs time scale using a streak camera system (see Figure 5E and SI part 7 for details), which only show a minimal decrease. Such slow decay further confirmed the assignment of this emission band to the spin forbidden doped Mn^{2+} $^4T_1$ to $^6A_1$ transition.

Moreover, using a longer excitation wavelength at 365 nm, the sample showed only blue emission (the optical image in Figure 5B inset). The observation of the blue emission, instead of the orange emission, could be explained by their different PLE spectra. The PLE spectrum of the orange emission approaches baseline at excitation wavelength longer than 330 nm (black trace in Figure 5A), while the PLE spectrum of the blue emission resembled the band gap absorption spectra of the ZnS QRs at short UV range (<320 nm), with additional intensities at long-wave UV range (320−420 nm) (black trace in Figure 5B). This observation indicates that the blue emission could be attributed to either the energy transfer from the host ZnS conduction band to the surface states or the direct excitation of surface states.[26,32] Furthermore, when the excitation wavelength varied from 300 to 400 nm, the blue emission band exhibits a gradual red shift from 400 to 460 nm (see Figures S20 and S21). This red shift could be explained by the heterogeneity of the surface states and relaxation of the vibrational states in both the electronic excitated and ground states (Figure 5G). Moreover, these surface states could act as the efficient electron hole recombination centers that have a very short emission decay lifetime of ~0.31 ns, as revealed by spectral resolved emission dynamics from the streak camera study (Figure 5D, and Figures S24 and S26). The decay of the blue emission is 10^7 fold faster than that of the orange emission.

It is worth noting that tunable dual-color emissions from $Zn_{1-x}Mn_xSe/ZnCdSe$ core/shell QDs has been reported, where

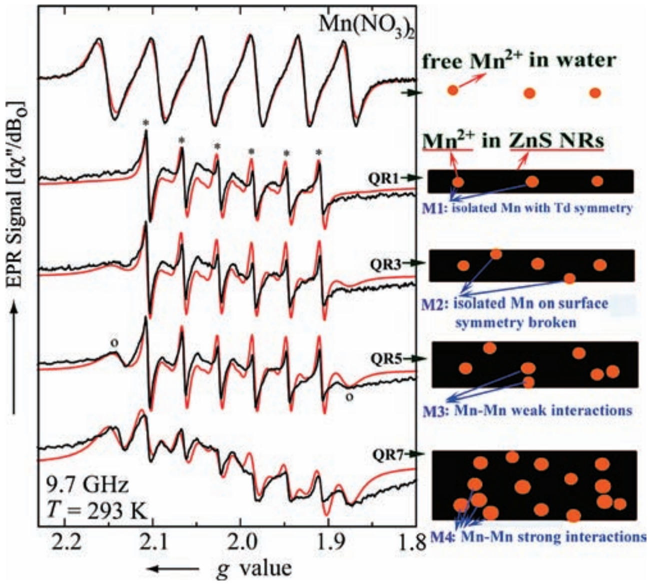

Figure 3. Electron paramagnetic resonance (EPR) spectroscopic characterization of Mn-doped ZnS QRs. Room temperature EPR spectra (black), simulation (red) and the corresponding schematic representation of Mn-doped QR samples with various diameters and doping levels: QR1, QR3, QR5, QR7, respectively. The EPR spectrum of 1 mM $Mn(NO_3)_2$ in aqueous solution is shown for comparison. Four different scenarios are illustrated for Mn^{2+} ions doped in the ZnS QRs. M1: isolated Mn^{2+} ions with symmetric tetrahedral coordination to sulfur, i. e. Mn^{2+} doped inside the ZnS QRs with symmetric tetrahedral coordination; M2: isolated Mn^{2+} with asymmetric tetrahedral coordination, i.e. Mn^{2+} doped on the surface of ZnS QRs; M3: weak dipole−dipole interaction between Mn^{2+} ions with intermediate Mn^{2+} doping level; M4: strong exchange coupling interaction between Mn^{2+} with high doping level.

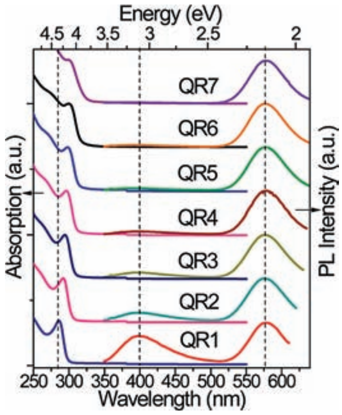

Figure 4. Optical characterization of Mn-doped ZnS QRs. (left) UV−vis absorption spectra of the series of Mn-doped ZnS QRs. The first absorption band position (Table 1) shows a gradual red shift with increase in QR diameter. (Right) Room-temperature photoluminescent emission spectra with UV excitation at 300 nm (PL intensity normalized at 585 nm). To collect the PL emission spectra for excitation at 300 nm, a long pass filter (320 nm) was placed in front of the detector monochromator.

their emission color (orange and green) could be tuned by changing the temperature between 210 and 400 K.[33] Very recently, the blue and orange dual-color emissions from the Mn-doped CdS/ZnS core/shell QDs have demonstrated to be controlled by varying the excitation intensity.[34] In contrast, the color (blue and orange) tuning of our Mn^{2+} doped ZnS QRs is controlled by using different excitation wavelengths at room temperature.

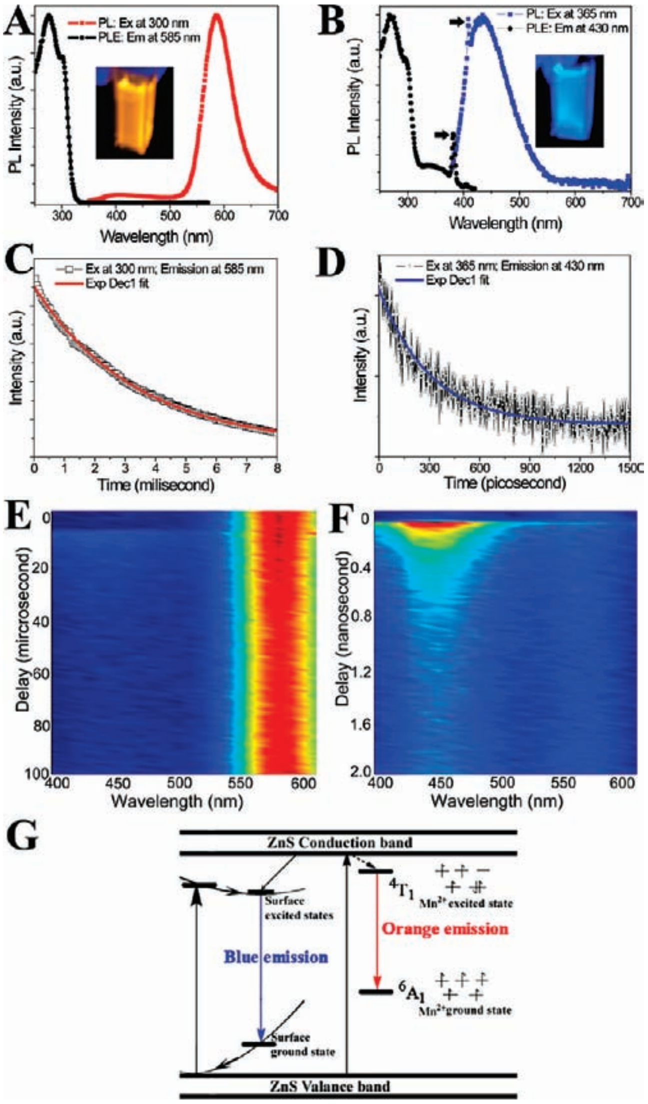

Figure 5. Tunable dual emissions of Mn-doped ZnS QRs (sample QR4). (**A**) PLE (black) and PL (red) spectra of QRs with emission monitored at 585 nm and excitation at 300 nm, respectively; (**B**) PLE (black) and PL (blue) spectra of the same sample with emission at 430 nm and excitation at 365 nm, respectively; (**C**) phosphorescence decay curve (black) and its fitting curve (red) with excitation at 300 nm; (**D**) lifetime decay curve derived from the streak camera (black) and its fitting curve (blue) with excitation at 365 nm; (**E**) Time evolution of the PL spectrum excitated with 325 nm pulsed laser (130 fs, 10 kHz). (**F**) Time evolution of the PL spectrum for the same sample excitated with 365 nm pulsed laser (130 fs, 250 kHz); (**G**) schematic energy profile of electronic structures in the Mn-doped ZnS QRs for illustration of the two distinct emission mechanisms. The dark arrows in **B** indicate the Raman signals from the hexane solvent. Insets of **A** and **B**: optical images of the samples in a quartz cuvette exposed to short-wave and long-wave UV, respectively. All the measurements were performed at room temperature.

Our doped QRs exhibited bright multiphoton excitation luminescence. We studied the multiphoton luminescence for the QR samples using femtosecond laser excitation with tunable

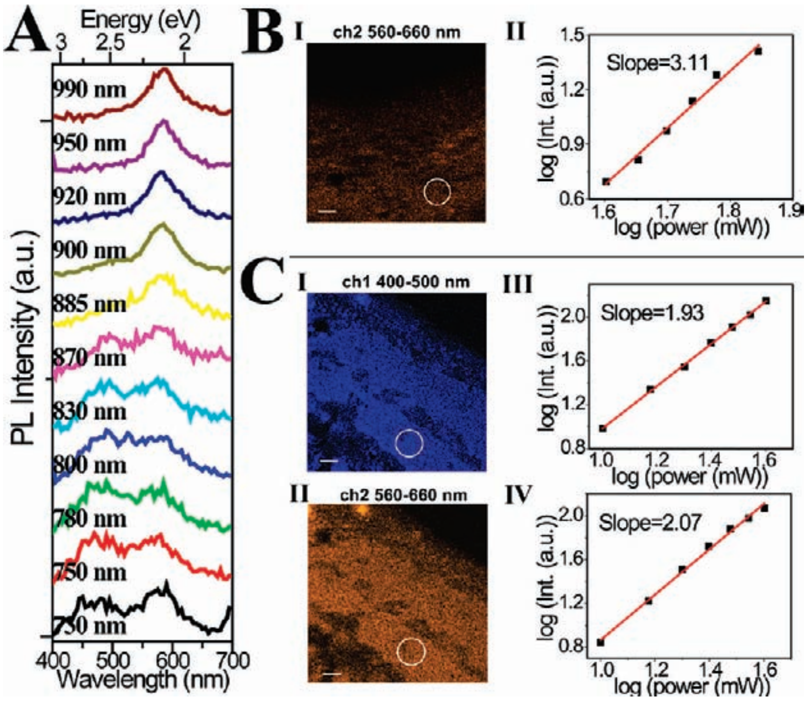

Figure 6. Multiphoton luminescence of the Mn-doped ZnS QRs. (**A**) Emission spectra from the Mn-doped ZnS QR sample (QR4) spin coated on a cover slide, with a range of laser excitation wavelengths from 990 to 730 nm using λ-scan mode. (**B**) With 950 nm laser excitation: (I) multiphoton luminescence image acquired between 560 and 660 nm (Ch2); (II) dependence of the luminescence intensity on the excitation power from the circled area in (I), obtained by decreasing the excitation power from 1.56 mW to 0.89 mW at the sample; lower power was used to avoid saturation. (**C**) With 730 nm laser excitation: (I) luminescence image acquired between 400 and 500 nm (Ch1); (II) luminescence image acquired between 560 and 660 nm; the color of the image was assigned according to the emission peak position. (III) and (IV) dependence of the luminescence intensity on the excitation power from the same circled area in (I) and (II), obtained by decreasing the excitation power from 1.84 mW to 0.46 mW at the sample. The scale bars in the images are 5 μm. Note that the powers labeled in the x-axis of BII, CIII and IV are the laser power before the microscope (for example, 1.56 mW at sample corresponds to ~70 mW before the microscope). It will not affect the value of slopes in the double "log" plot here.[42]

wavelength ranging from 990 to 730 nm (Figure 6A, S29–S36). Specifically, using 950 nm laser excitation and λ-scan imaging (Figure 6BI), a strong luminescence with a single peak centered at 585 nm was observed (purple trace in Figure 6A). In addition, when the excitation wavelength was tuned from 990 to 900 nm, the emission spectra were dominated by the 585 nm emission. The cubic dependence of the signal intensity on the excitation power (Figure 6B-II) confirmed that this emission is three-photon excitation luminescence (3PL).This indicates the orange emission observed here arise from the energy transfer from the three-photon excitated host ZnS conduction band to the doped Mn^{2+} $^4T_1$ state.

With 730 nm excitation and λ-scan imaging, dual luminescence spectra (Figure 6A, black trace) with two bands centered at 450 nm (Figure 6C-I) and 585 nm (Figure 6C-II) were obtained. The quadratic dependence of the signal intensity on the excitation power for both channels (Figure 6C-III,IV) confirmed two-photon luminescence (2PL). When intermediate wavelengths (from 800 to 885 nm) were used for excitation, power dependences of the emission were in between two and three, indicating a mixed 2PL and 3PL behavior (Figures S29–S36). Two-photon upconversion luminescence of Mn^{2+} in doped ZnS bulk and nanoparticles were reported by Chen and co-workers[35] using a fixed excitation at 767 nm. The multiphoton luminescence for the QR samples observed here using tunable excitation wavelength ranging from 990 to 730 nm demonstrated that the Mn-doped ZnS QRs could be promising bio-imaging labels in multiphoton excitation microscopy using a near-infrared (NIR) laser source, which has the advantages of deep tissue penetration and low photo-damaging effects.[36,37]

■ CONCLUSIONS

In summary, we have demonstrated the synthesis of high-quality Mn-doped ZnS QRs with finely tunable diameters and doping levels using a simple, fast, and green phosphine-free colloidal chemistry. The location and the interaction of the paramagnetic Mn ions doped in the host ZnS QRs were investigated by EPR spectroscopy with modeling. The obtained Mn-doped ZnS QRs exhibit tunable dual-color emissions and three- and two-photon excitation upconversion luminescence, which make them valuable to a wide range of applications including photonic displays, sensors, lasers and biological imaging.

■ EXPERIMENTAL SECTION

Chemicals. Zinc nitrate tetrahydrate ($Zn(NO_3)_2 \bullet 4H_2O$, 99.8%), Manganese nitrate hydrate ($Mn(NO_3)_2 \bullet xH_2O$, 99.99%), sulfur (S, 99.998% powder), oleylamine (OAm, technical grade, 70%), 1-Dodecanethiol (DDT, ≥98%), methanol (≥99.5%), ethanol (>99%), isopropyl alcohol (IPA, 99%), and hexane (≥95%), and Coumarin 480 were purchased from Sigma-Aldrich and used without further purification.

Synthesis. Our strategy to synthesize Mn-doped ZnS QRs is based on phosphine-free colloidal chemistry, with the advantages of being fast, simple and environmental friendly.[32,38–40] The synthesis of Mn-doped

ZnS QRs for a typical sample with a diameter of 2.0 nm (sample QR2): First, S precursor solution was prepared by dissolving 4 mmol of S powder in 20 mL OAm and holding the solution at 100 °C; then the solution was continuously stirred for 2 h before use. Second, Zn/Mn-OAm complex precursor solution was prepared by adding 0.4 mmol of $Zn(NO_3)_2$, 0.02 mmol of $Mn(NO_3)_2$, and 0.5 mL of DDT to 15 mL OAm in a flask, which was kept at 160 °C and stirred until a uniform mixture was formed. Third, 2 mL of S-precursor solution was quickly injected into the Zn/Mn-OAm precursor solution through a syringe with continuous stirring. After injection, the temperature was raised to 230 °C with a temperature ramp of 15 °C per minute. After 10 min at 230 °C (timing started once the temperature was reached), the solution mixture was removed from the heating mantle, and mixed with cold methanol (3 equivalents), ethanol (3 equivalents), and isopropyl alcohol (3 equivalents). Unreacted starting materials were removed by centrifugation (3,000 rpm for 30 min at 4 °C) and the samples were redispersed in hexane (1 equivalent). The centrifugation and re-dispersion were repeated three times. The synthesis of Mn doped ZnS QRs with various Mn levels and diameters was achieved by changing the starting Mn^{2+} concentration and reaction times as summarized in Table 1, while keeping the other experimental parameters the same. The final products were redispersed in hexane for characterizations.

Characterization. Samples for TEM analysis were prepared by dropping a diluted hexane solution of doped QRs onto the ultrathin carbon-coated copper grids and air-dried. TEM, HRTEM, HAADF-STEM, and energy dispersive X-ray spectroscopy (EDS) were performed on a JEOL JEM 2010F electron microscope operating at 200 kV. For the powder XRD measurements, the QR samples were dried on a quartz substrate, and it was performed on a PANalytical X'Pert Pro Materials Research X-ray Diffractometer with Cu Kα radiation (λ = 1.5418 Å) and scanned at a rate of 0.025 deg/s.

ICP-MS was performed on a Thermo X-series Q-ICP-MS with CCT (Collision Cell Technology) instrument. Mn was measured at 55Mn, while Zn was measured at 64Zn, 66Zn and 68Zn. The Zn isotope with the lowest detection limit (66Zn) was selected for reporting, but all three isotopes gave values within 5% of each other. Two standard checks and a blank were measured for every four sample analyses, and each sample was measured for at least three different dilutions. The variation of the Zn/Mn ratio measured in two separate dilutions for each sample was always less than 3%, and typically less than 1.3%. The doping level of Mn in the ZnS QRs was calculated from the atomic ratio of the Mn/(Mn+Zn) measured.

UV−vis absorption spectra were recorded at room temperature with a JASCO V670 spectrophotometer. Photoluminescence spectra were measured at room temperature using a NanoLog fluorescence-spectrometer manufactured by HORIBA Jobin Yvon equipped with a thermoelectric cooled PMT (R928 in the range 200−850 nm), a 450 W xenon short-arc lamp, and a flash lamp (for phosphorescence decay lifetime). The emission spectra obtained were corrected using a response file that records the sensitivity of the PMT to different wavelengths of light generated using a standard lamp. The excitation spectra were corrected using the signal from the reference photodiode that records the variation of the intensity of the lamp with excitation wavelength.

EPR study was performed at the EPR Facility at Arizona State University. EPR spectra were recorded at room temperature using a Bruker ELEXSYS 580 X-band spectrometer (Bruker, Silberstreifen, Germany) equipped with a cylindrical mode resonator (Bruker, ER 4103TM) designed for aqueous and high-dielectric samples. Samples were placed in a flat, quartz cell, which was mounted in the resonator. The parameters used were: magnetic field modulation frequency 100 kHz, amplitude 1 mT, microwave power 10 mW, microwave frequency 9.7 GHz and the sweep time 84 s. The spectra were obtained by averaging 8−12 scans.

The time-resolved PL spectroscopic study was performed on a system consisting of an ultrafast laser and streak camera detection system. The intensity of PL as a function of emission wavelength and time for the Mn-doped ZnS QRs samples was recorded simultaneously. The 130-fs light pulses at 650, 700, or 730 nm were generated from a visible OPA pumped by a femtosecond regenerative amplifier system operating between 10 and 250 kHz (Coherent Laser Inc., Verdi 18, Mira900, RegA9000, OPA9400). The laser radiation was then frequency-doubled in a single pass configuration within a nonlinear crystal to produce femtosecond UV radiation at 325, 350, and 365 nm.

A femtosecond laser (Maitai, Spectra-Physics, Fremont, CA) with 130-fs pulse and 80 MHz repetition rate, tunable within 690−1020 nm, was used as the excitation source for multiphoton imaging. The laser beam was sent into a FV1000 laser-scanning microscope (Olympus America Inc., PA) and focused onto thr sample with a 60X/IR water objective lens (NA = 1.2). The backward multi-photon signals were collected using the same objective, separated from the excitation laser by a dichroic mirror and detected by two internal spectral detectors (channel 1 and channel 2). The detection range was set as 400−500 nm for channel 1 and 560−660 nm for channel 2, separated by a diachronic mirror (SD560). Microspectroscopy was performed by λ-scan using the internal spectral detector in the confocal scanning box. Details of the optical setup can be found elsewhere.[41,42]

■ ASSOCIATED CONTENT

Ⓢ **Supporting Information.** Additional discussions, Figures S1−36, Movie S1. This material is available free of charge via the Internet at http://pubs.acs.org.

■ AUTHOR INFORMATION

Corresponding Author

yan_liu@asu.edu

■ ACKNOWLEDGMENT

We thank Dr. G. Gordon for technical assistance with ICP-MS measurements. We thank Prof. K. Redding and Dr. L. Cao for insightful discussions. We thank J. Nangreave for help proofreading the manuscript. The use of facilities within the Center for Solid State Science at ASU is also acknowledged. We thank funding supports from ONR, ARO, NSF, NIH to Y. L. and supports from ONR, NSF, NIH, ARO, DOE and Sloan Research Fellowship to H.Y.; Y.L and H.Y. was also supported as part of the Center for Bio-Inspired Solar Fuel Production, an Energy Frontier Research Center funded by the U.S. Department of Energy, Office of Science, Office of Basic Energy Sciences under Award Number DE-SC0001016.

■ REFERENCES

(1) Peng, X. G.; Manna, L.; Yang, W. D.; Wickham, J.; Scher, E. C.; Kadavanich, A.; Alivisatos, A. P. *Nature* **2000**, *404*, 59.

(2) Li, L. S.; Hu, J. T.; Yang, W. D.; Alivisatos, A. P. *Nano Lett.* **2001**, *1*, 349.

(3) Peng, Z. A.; Peng, X. G. *J. Am. Chem. Soc.* **2001**, *123*, 1389.

(4) Huynh, W. U.; Dittmer, J. J.; Alivisatos, A. P. *Science* **2002**, *295*, 2425.

(5) Kan, S.; Mokari, T.; Rothenberg, E.; Banin, U. *Nat. Mater.* **2003**, *2*, 155.

(6) Yin, M.; Gu, Y.; Kuskovsky, I. L.; Andelman, T.; Zhu, Y.; Neumark, G. F.; O'Brien, S. *J. Am. Chem. Soc.* **2004**, *126*, 6206.

(7) Fu, A.; Gu, W.; Boussert, B.; Koski, K.; Gerion, D.; Manna, L.; Gros, M. L.; Larabell, C. A.; Alivisatos, A. P. *Nano Lett.* **2007**, *7*, 179.

(8) Wang, F. D.; Buhro, W. E. *J. Am. Chem. Soc.* **2007**, *129*, 14381.

(9) Chen, J. S.; Tan, Y. L.; Li, C. M.; Cheah, Y. L.; Luan, D. Y.; Madhavi, S.; Boey, F. Y. C.; Archer, L. A.; Lou, X. W. *J. Am. Chem. Soc.* **2010**, *132*, 6124.

(10) Zhuang, Z. B.; Lu, X. T.; Peng, Q.; Li, Y. D. *J. Am. Chem. Soc.* **2010**, *132*, 1819.

(11) Beaulac, R.; Ochsenbein, S. T.; Gamelin, D. R. . In *Semiconductor Quantum Dots*; Klimov, V. I., Ed.; CRC Press: Boca Raton, FL, 2010; pp 397.

(12) Norris, D. J.; Yao, N.; Charnock, F. T.; Kennedy, T. A. *Nano Lett.* **2001**, *1*, 3.

(13) Erwin, S. C.; Zu, L.; Haftel, M. I.; Efros, A. L.; Kennedy, T. A.; Norris, D. J. *Nature* **2005**, *436*, 91.

(14) Yang, Y.; Chen, O.; Angerhofer, A.; Cao, Y. C. *J. Am. Chem. Soc.* **2006**, *128*, 12428.

(15) Dalpian, G. M.; Chelikowsky, J. R. *Phys. Rev. Lett.* **2006**, *96*, 226802.

(16) Norris, D. J.; Efros, A. L.; Erwin, S. C. *Science* **2008**, *319*, 1776.

(17) Pradhan, N.; Goorskey, D.; Thessing, J.; Peng, X. G. *J. Am. Chem. Soc.* **2005**, *127*, 17586.

(18) Pradhan, N.; Peng, X. G. *J. Am. Chem. Soc.* **2007**, *129*, 3339.

(19) Pradhan, N.; Battaglia, D. M.; Liu, Y. C.; Peng, X. G. *Nano Lett.* **2007**, *7*, 312.

(20) Thakar, R.; Chen, Y. C.; Snee, P. T. *Nano Lett.* **2007**, *7*, 3429.

(21) Chakraborty, A. N. S.; Sarma, D. D. *J. Am. Chem. Soc.* **2008**, *130*, 10605.

(22) Yang, Y. A.; Chen, O.; Angerhofer, A.; Cao, Y. C. *J. Am. Chem. Soc.* **2008**, *130*, 15649.

(23) Viswanatha, R.; Battaglia, D. M.; Curtis, M. E.; Mishima, T. D.; Johnson, M. B.; Peng, X. G. *Nano Res.* **2008**, *1*, 138.

(24) Chen, D.; Viswanatha, R.; Ong, G. L.; Xie, R.; Balasubramaninan, M.; Peng, X. G. J. *Am. Chem. Soc.* **2009**, *131*, 9333.

(25) Srivastava, B. B.; Jana, S.; Karan, N. S.; Paria, S.; Jana, N. R.; Sarma, D. D.; Pradhan, N. *J. Phys. Chem. Lett.* **2010**, *1*, 1454.

(26) Biswas, S.; Kar, S.; Chaudhuri, S. *J. Phys. Chem. B* **2005**, *109*, 17526.

(27) Li, P.; Wang, L. Y.; Wang, L.; Li, Y. D. *Chem.—Eur. J.* **2008**, *14*, 5951.

(28) Chin, P. T. K.; Stouwdam, J. W.; Janssen, R. A. J. *Nano Lett.* **2009**, *9*, 745.

(29) Borse, P. H.; Srinivas, D.; Shinde, R. F.; Date, S. K.; Vogel, W.; Kulkarni, S. K. *Phys. Rev. B* **1999**, *60*, 8659.

(30) *Diluted Magnetic Semiconductors*; Furdyna, J. K.; Kossut, J., Eds.; Academic: New York, 1988.

(31) Peng, X. G.; Wickham, J.; Alivisatos, A. P. *J. Am. Chem. Soc.* **1998**, *120*, 5343.

(32) Deng, Z.; Yan, H.; Liu, Y. *Angew. Chem., Int. Ed.* **2010**, *49*, 8695.

(33) Vlaskin, V. A.; Janssen, N.; Rijssel, J. V.; Beaulac, R.; Gamelin, D. R. *Nano Lett.* **2010**, *10*, 3670.

(34) Chen, O.; Shelby, D. E.; Yang, Y.; Zhuang, J.; Wang, T.; Niu, C.; Omenetto, N.; Cao, Y. C. *Angew. Chem., Int. Ed.* **2010**, *49*, 10132.

(35) Chen, W.; Joly, A. G.; Zhang, J. Z. *Phys. Rev. B* **2001**, *64*, 041202.

(36) Cao, L.; Wang, X.; Meziani, M. J.; Lu, F.; Wang, H.; Luo, P. G.; Lin, Y.; Harruff, B. A.; Veca, L. M.; Murray, D.; Xie, S. Y.; Sun, Y. P. *J. Am. Chem. Soc.* **2007**, *129*, 11318.

(37) Larson, D. R.; Zipfel, W. R.; Williams, R. M.; Clark, S. W.; Bruchez, M. P.; Wise, F. W.; Webb, W. W. *Science* **2003**, *300*, 1434.

(38) Deng, Z. T; Cao, L.; Tang, F. Q.; Zou, B. S. *J. Phys. Chem. B* **2005**, *109*, 16671.

(39) Deng, Z. T.; Yan, H.; Liu, Y. *J. Am. Chem. Soc.* **2009**, *131*, 17744.

(40) Deng, Z. T.; Mansuripur, M; Muscat, A. J. *Nano Lett.* **2009**, *9*, 2015.

(41) Chen, H.; Wang, H.; Slipchenko, M. N.; Jung, Y.; Shi, Y.; Zhu, J.; Buhman, K. K.; Cheng, J. X. *Opt. Express* **2009**, *17*, 1282.

(42) Tong, L.; Cobley, C. M.; Chen, J. Y.; Xia, Y. N.; Cheng, J. X. *Angew. Chem., Int. Ed.* **2010**, *49*, 3485.